Nano Research 2015, 8(10): 3365–3371
DOI 10.1007/s12274-015-0836-5
Research Article
ISSN 1998-0124
CN 11-5974/O4

Three-dimensional porous superaerophobic nickel nanoflower electrodes for high-performance hydrazine oxidation

Guang Feng[1,§], Yun Kuang[1,§], Yingjie Li[1], and Xiaoming Sun[1,2] (✉)

[1] *State Key Laboratory of Chemical Resource Engineering, Beijing University of Chemical Technology, Beijing 100029, China*
[2] *Institute for New Energy Materials & Low-Carbon Technologies, Tianjin University of Technology, Tianjin 300384, China*
[§] *These authors contributed equally to this work.*

Received: 17 April 2015
Revised: 3 June 2015
Accepted: 9 June 2015

KEYWORDS
three-dimensional (3D) porous,
Ni nanoflower,
electrocatalysis,
ultra-high stability

ABSTRACT

Finding inexpensive electrodes with high activity and stability is key to realize the practical application of fuel cells. Here, we report the fabrication of three-dimensional (3D) porous nickel nanoflower (3D-PNNF) electrodes via an *in situ* reduction method. The 3D-PNNF electrodes have a high surface area, show tight binding to the electroconductive substrate, and most importantly, have superaerophobic (bubble repellent) surfaces. Therefore, the electrocatalytic hydrazine oxidation performance of the 3D-PNNF electrodes was much higher than that of commercial Pt/C catalysts because of its ultra-weak gas-bubble adhesion and ultra-fast gas-bubble release. Furthermore, the 3D-PNNF electrodes showed ultra-high stability even under a high current density (260 mA/cm^2), which makes it promising for practical applications. In addition, the construction of superaerophobic nanostructures could also be beneficial for other gas evolution processes (e.g., hydrogen evolution reaction).

1 Introduction

The perpetually increasing environmental issues and the depletion of fossil resources have stimulated considerable effort to exploit low-cost, clean, efficient, and renewable alternative power sources [1–5]. Fuel cells (FCs), which enable the direct conversion of chemical energy into electrical energy through the oxidation of renewable fuels, have been considered as ideal alternative power sources for future mobile and stationary applications owing to their high energy densities and power densities [6–11].

However, their high usage of expensive noble-metal catalysts and the sluggish kinetics of their electrocatalytic oxidation are two key obstacles hampering the commercial viability of FCs [12–15]. In addition, the stability of noble-metal-based catalysts is a serious problem because of the potential dissolution/aggregation of active materials during the catalytic reactions [9, 16], which greatly shortens the life time of FCs.

Address correspondence to sunxm@mail.buct.edu.cn

In the electrocatalytic hydrazine oxidation reaction in direct hydrazine FCs, non-noble metals [17–19] (e.g., Cu, Ni, etc.) and their alloys [20–22] have been reported to show activities as high as those of noble metals [23–25]. Furthermore, such materials show even higher electrocatalytic performances when fabricated in the nanoscale [19, 26], making them potential alternatives for noble-metal-based catalysts in direct hydrazine FCs.

Structural electrodes, which have three-dimensional (3D) porous morphology, ultra-high surface area, and a specific crystalline structure, have shown advantages in electrocatalytic oxidation owing to their well-controlled structure and composition [27–30]. Among the various existing methods for controlling the structure, only chemical bath deposition (CBD) and E-beam deposition could achieve the nano-sized deposition of non-noble transition metals with controlled sizes [31, 32]; however, the structure control of these relatively active metals is still a significant issue.

Herein, we report the fabrication of 3D porous nickel nanoflower (3D-PNNF) electrodes through an *in situ* reduction method. The electrocatalytic hydrazine oxidation performance of the fabricated 3D-PNNF electrodes was much higher than that of commercial Pt/C catalysts owing to their superaerophobic (bubble repellent) surfaces with ultra-weak gas-bubble adhesion and ultra-fast gas-bubble release. Furthermore, the 3D-PNNF electrodes showed ultra-high stability even under a high current density (260 mA/cm^2), which makes it promising for practical applications.

2 Results and discussion

The 3D-PNNFs were prepared using an *in situ* conversion method, and the procedure is schematically shown in Fig. 1(a). First, $Ni(OH)_2$ nanosheet arrays were synthesized on nickel foam by following the method in our previous work [33]. Then, the as-formed $Ni(OH)_2$ nanosheet arrays were solvothermally reduced in ethylene glycol with the help of sodium borohydride [34] (see the Electronic Supplementary Material (ESM) for synthesis details).

The morphology of the obtained 3D-PNNF electrodes was characterized using a scanning electron microscope (SEM) and transmission electron microscope (TEM). Figures 1(a) and 1(b) show the morphology of the as-prepared samples. It can be seen that the synthesized $Ni(OH)_2$ nanosheet arrays show a porous structure, while Ni nanoflowers inherit the high porosity of $Ni(OH)_2$ nanosheet arrays after reduction. In contrast to the $Ni(OH)_2$ nanosheet precursor, the nanoflowers showed rough surfaces, as could be seen in the inset of Fig. 1(b). In addition, the nanoflowers were linked to each other with inner networks to form a stable structure. The high-resolution TEM (HRTEM) image shown in Fig. 1(c) reveals the flower-like morphology of the obtained product, and each flower was composed of several hexagonal Ni nanosheets to form a 3D porous structure with ultra-high surface areas. The enlarged HRTEM image shows a lattice spacing of 0.203 nm that can be indexed to the (111) plane of Ni nanocrystals, which agrees with the hexagonal nanosheet structure.

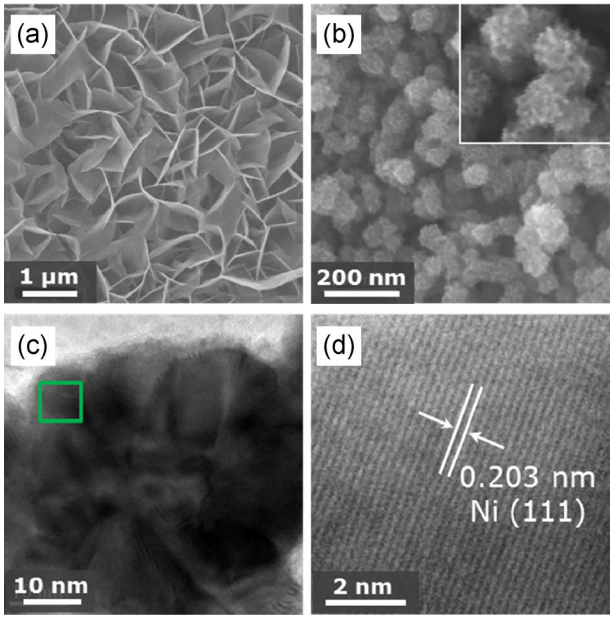

Figure 1 SEM image of (a) a $Ni(OH)_2$ nanosheet array and (b) Ni nanoflowers (inset shows enlarged SEM image of several nanoflowers). (c) HRTEM image of a single Ni nanoflower. (d) Enlarged HRTEM image of the region marked in (c).

The selective-area electron diffraction (SAED) pattern (Figs. 2(a) and 2(b)) of several Ni nanoflowers shows typical (111), (200), (220), (311), and (331) diffraction rings of well-crystalized Ni, confirming that the product was composed of Ni. It should be noted that the (111) ring was much brighter than the other diffraction rings, demonstrating the exposed (111) crystalline structure, which agreed with the HRTEM observation (Fig. 1(d)).

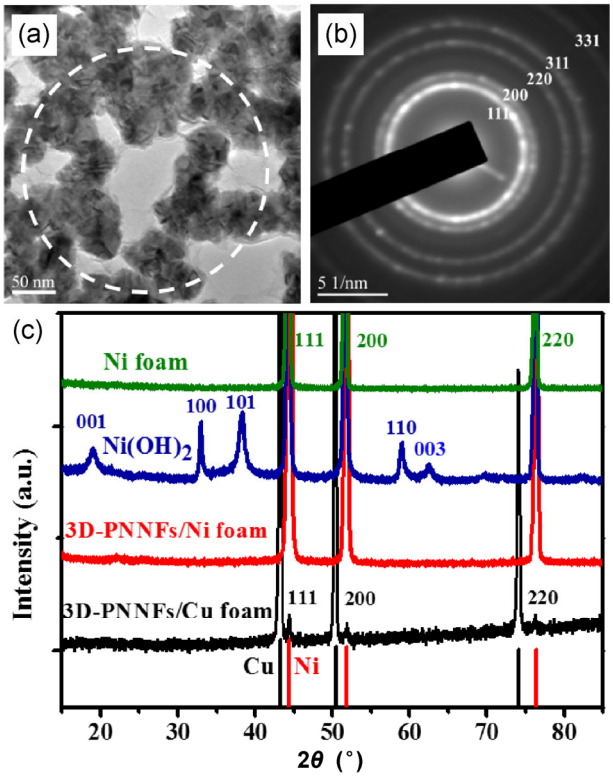

Figure 2 (a) TEM image of the Ni nanoflowers. (b) SAED pattern of the region marked in (a). (c) XRD pattern of the Ni foam substrate, $Ni(OH)_2$ nanosheet arrays, and Ni nanoflowers. The two lines at the base show standard XRD patterns of Cu and Ni.

For further confirmation that the as-obtained nanoflowers were indeed composed of Ni, powder X-ray diffraction (XRD) patterns of the samples were collected, as shown in Fig. 2(c). The Ni foam substrate shows well-crystallized Ni peaks before any treatment, but it exhibits typical $Ni(OH)_2$ peaks after the growth of the nanosheet arrays, confirming that the nanosheet arrays were composed of $Ni(OH)_2$. It should be noted that the width of the $Ni(OH)_2$ peaks are low, indicating good crystallization of the nanosheet arrays, which agreed with the SEM observation (Fig. 1(a)). After the reduction of the $Ni(OH)_2$ nanosheet arrays, the sample showed only Ni peaks with no remaining $Ni(OH)_2$ peaks, suggesting the full reduction of $Ni(OH)_2$. In order to confirm that the reduced product consisted of Ni while excluding the influence of the Ni substrate, we prepared the same 3D-PNNF sample on a Cu foam substrate (black line in Fig. 2(c)). The (111), (200), and (220) peaks of the Ni crystal could be clearly observed, confirming that the reduced nanoflowers were indeed composed of Ni.

Such 3D open porous but interconnected hierarchal networks endowed this electrode with ultra-high electrocatalytic hydrazine oxidation reaction performance (HzOR), which is even higher than that of commercial Pt/C catalysts.

Figure 3(a) shows the electrochemical behavior of the 3D-PNNF electrode in 3 M KOH solution with and without hydrazine. It could be seen from the linear sweep voltammetry (LSV) curve for the solution without hydrazine that the nickel started to be oxidized at 0.25 V by showing a rising anodic current (vs. reversible hydrogen electrode (RHE), also see inset for enlarged image); thus, the potential window was limited at –0.05–0.25 V. Figure 3(b) compares the catalytic performance of electrodes based on 3D-PNNFs, $Ni(OH)_2$ nanosheet array, pure Ni foam, and 20 wt.% Pt/C (loaded on Ni foam, loading amount of 1 mg/cm^2, which is 25% higher than that for Ni nanoflowers, 0.8 mg/cm^2) in a solution containing 0.5 M hydrazine. At a potential of 0.25 V, the 3D-PNNF electrode showed a considerable current density (198.6 mA/cm^2), which was 1.57 times higher than that of commercial Pt/C catalysts (126.2 mA/cm^2), while no obvious current (< 10 mA/cm^2) was observed on the Ni-foam electrode. This result indicates that the 3D-PNNF electrode exhibited ultra-high catalytic performance for the oxidation of hydrazine. The onset oxidation potential (E_{on}) of hydrazine was usually regarded as an evaluation criterion to compare the performances of catalysts. Here, the E_{on} of the Ni-nanoflower electrode was lower than that of the Pt/C electrode, which was more obvious in 0.1 M N_2H_4 and 1 M N_2H_4 (Fig. S1 in the ESM). Electrochemical impedance spectroscopy (EIS) was also considered a powerful tool to study the electrode kinetics in a catalytic reaction. As shown in Fig. 3(c), the Nyquist plots of the four electrodes under the same potential and semicircles indicates that hydrazine oxidation on the four electrodes followed a similar mechanism and was kinetically controlled. However, the 3D-PNNF electrode showed a much smaller charge-transfer resistance (~0.7 Ω) than that of the electrodes based on Pt/C (~1.4 Ω) and the $Ni(OH)_2$ nanosheet array (~11.9 Ω), demonstrating accelerated kinetics for hydrazine oxidation. In addition to specific activity, stability is an important parameter to judge the actual performance of an electrode material. To evaluate the

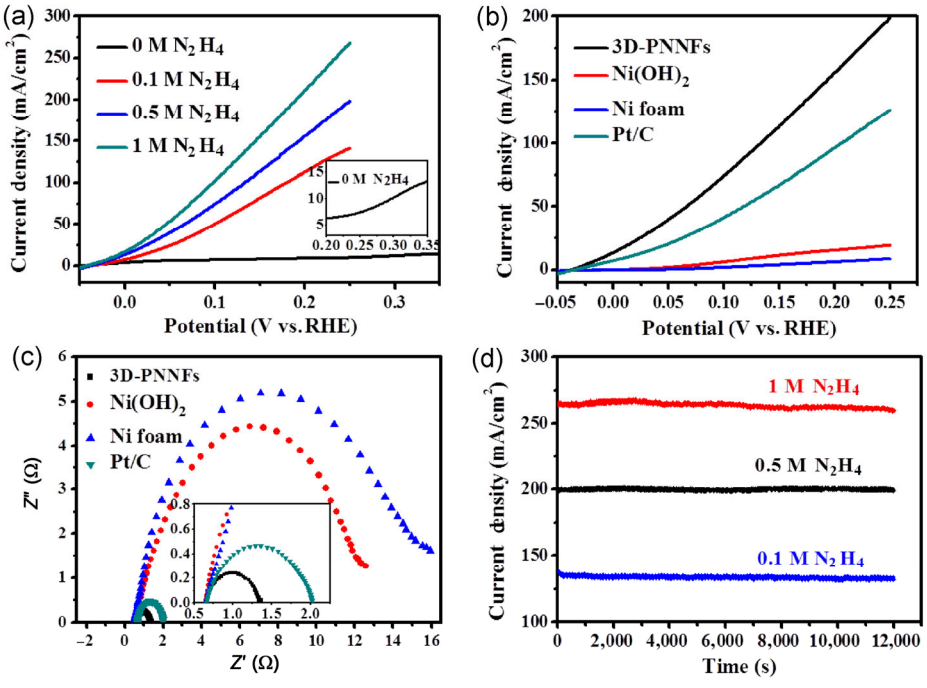

Figure 3 (a) HzOR performance of Ni nanoflowers at different hydrazine concentrations (inset shows an enlarged curve of 0 M N_2H_4). (b) HzOR performance of 3D Ni nanoflowers, $Ni(OH)_2$ nanosheet array, pure Ni foam, and 20 wt.% Pt/C (loaded on Ni foam) electrodes. (c) Nyquist plots of the four electrodes, indicating that the charge-transfer resistance of Ni nanoflowers is much smaller than that of the other electrodes. (d) Stability testing of Ni nanoflowers at different current densities.

stability of the high-performance 3D-PNNF electrode, long-term stability for 12,000 s was assessed under a constant potential (0.25 V) in different concentrations of hydrazine (i.e., different current densities), as shown in Fig. 3(d). Even under a high current density (260 mA/cm^2), the 3D-PNNF electrodes could maintain a current density above 98% of its initial current density, while at a lower current density, the Ni nanoflowers maintained a current density near 100% of its initial current density after 12,000 s, confirming the good stability of the 3D-PNNF electrode. It should also be noted that even under a higher potential (0.35 V, current density of 360 mA/cm^2) at which Ni might be oxidized, the 3D-PNNF electrode showed a current density greater than 95% of its initial current density after 12,000 s (Fig. S2 in the ESM), possibly because the Ni nanoflowers were too active for hydrazine oxidation and protected the catalytic material from oxidation. Such ultra-high stability makes this electrode highly suitable for the commercialization of low cost, highly efficient direct hydrazine FCs.

The reasons for the high electrocatalytic performance and ultra-high stability of the 3D-PNNF electrode were the tight binding between the active material and substrate, low resistance of the inter-connected network, and fast mass transfer on superaerophobic [26] surfaces. Therefore, the supply of raw materials (i.e., hydrazine) and release of products (i.e., N_2) were fast; meanwhile, no electrocatalytic active sites were blocked and less catalytic active materials (i.e. surface atoms) were hauleded by the adhesion of intermediates or products.

In order to verify the hypothesis that the 3D-PNNF electrode was superaerophobic, adhesion-force tests were performed on the four abovementioned electrodes. As shown in Fig. 4(a), the 3D-PNNF electrode showed little adhesion force (approximately 5.5 μN) to the gas bubbles; in contrast, the adhesion force of the Pt/C electrode was almost 10 times higher (approximately 51 μN). The different adhesive properties would lead to different gas releasing behaviors in hydrazine oxidation (i.e., N_2 evolution) reaction. The superaerophobic 3D-PNNF electrode showed little adhesion force and, thus, resulted in a small releasing size (average size of bubbles < 50 μm) and fast removal of the as-formed N_2 gas bubbles at high reaction rates (Fig. 4(b) and Fig. S3(a) in the ESM). However, the

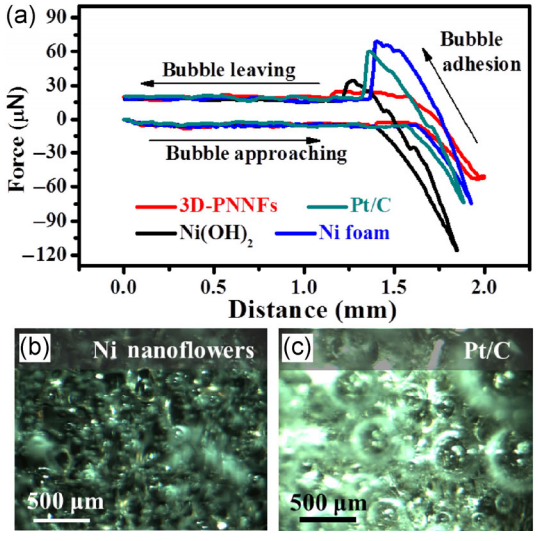

Figure 4 (a) Measurement of adhesive forces of the gas bubbles on 3D Ni nanoflowers, $Ni(OH)_2$ nanosheet array, pure Ni foam, and 20 wt.% Pt/C (loaded on Ni foam) electrodes, demonstrating that the 3D Ni nanoflowers afford an extremely small bubble adhesive force and underwater "superaerophobic" surface. Digital images of the bubble generation behavior on (b) 3D Ni nanoflowers and (c) Pt/C (loaded on Ni foam) electrodes.

large adhesion force of gas bubbles on Pt/C-Ni foam resulted in the severe blockage of electrocatalytic active sites from hydrazine, resulting in a much bigger releasing size (average size of bubbles > 150 μm) of bubbles (Fig. S3(b) in the ESM) and relatively low electrocatalytic performance.

In order to visualize the gas-releasing process and to obtain a thorough comparison, digital recording processes were performed on the superaerophobic 3D-PNNF electrode and Pt/C-Ni foam electrodes at the same current density (~60 mA/cm^2) for hydrazine oxidation (Movies S1 and S2 in the ESM). It is observed that the bubbles were generated and removed quickly before they grew larger at the superaerophobic 3D-PNNF surface (Movie S1 in the ESM). However, for Pt/C-Ni foam electrodes, the as-formed N_2 bubbles became larger much more slowly and adhered strongly to the electrode surface (Movie S2 in the ESM). The bubbles left the electrode surface only when the size of the gas bubbles increased sufficiently to overcome the high adhesion force. These results further confirmed that the high electrocatalytic performance was a result of superaerophobic surfaces along with high intrinsic activity.

The 3D-PNNF electrode with superaerophobic surfaces could also increase the performance of the hydrogen evolution reaction (HER). As shown in Fig. 5(a), the onset overpotential (η) of the 3D-PNNF

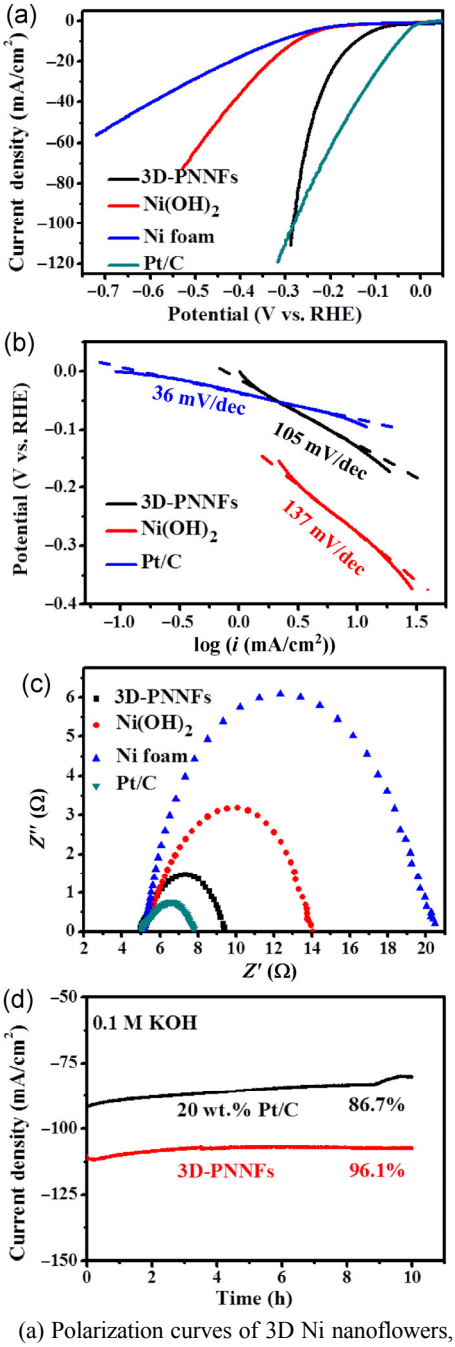

Figure 5 (a) Polarization curves of 3D Ni nanoflowers, $Ni(OH)_2$ nanosheet array, pure Ni foam, and 20 wt.% Pt/C (loaded on Ni foam) electrodes. (b) Tafel plots on 3D Ni nanoflowers (black), $Ni(OH)_2$ nanosheet array (red) and 20 wt.% Pt/C electrodes (blue). (c) Nyquist plots of the four electrodes. (d) Stability testing of 3D Ni nanoflowers and 20 wt.% Pt/C electrodes under constant potentials in 0.1 M KOH solution. This result indicates that the electrode based on 3D Ni nanoflowers shows an outstanding stability for HER.

electrode was much lower than that of $Ni(OH)_2$ nanowall film and pure Ni foam. Although the onset potential of the 3D-PNNF electrode was more negative than that of the Pt/C catalyst, the current density increased much faster and exceeded the Pt/C catalyst at a low potential, although Pt/C had the lowest charge-transfer resistance, as could be seen from the corresponding Tafel slopes (Fig. 5(b)) and Nyquist plots (Fig. 5(c)). This result suggested that the surface structure of the electrode is even more important than the intrinsic activity of active materials, which is consistent with our previous observation on a MoS_2 nanoarray [35]. Besides, the superaerophobic structure also provides the 3D-PNNF electrode with high stability for the same reason as the ultra-high HzOR stability (Fig. 5(d)).

3 Summary

We fabricated 3D-PNNF electrodes through a solvothermal *in situ* conversion method from $Ni(OH)_2$ nanosheet array precursors. The 3D-PNNF electrode showed superaerophobic surfaces and, therefore, exhibited excellent gas evolution performance (hydrazine oxidation and hydrogen evolution) owing to ultra-fast gas-bubble release. Furthermore, a low gas-bubble adhesion force and strong interaction between catalytic active materials and substrates provide ultra-high stability in the 3D-PNNF electrode even under a high current density. This synthesis strategy opens an avenue for structure control in non-noble-metal nanostructures and will be significantly beneficial for the commercialization of low cost, highly efficient, and ultra-stable FCs.

Acknowledgements

This work was supported by the National Natural Science Foundation of China (Nos. 21271018 and 21125101), the National Basic Research Program of China (No. 2011CBA00503), the National High-tech R&D Program of China (No. 2012AA03A609) and the Program for Changjiang Scholars and Innovative Research Team in University.

Electronic Supplementary Material: Supplementary material (experimental details, supplementary figures and movies) is available in the online version of this article at http://dx.doi.org/ 10.1007/s12274-015-0836-5.

References

[1] Lewis, N. S.; Nocera, D. G. Powering the planet: Chemical challenges in solar energy utilization. *Proc. Natl. Acad. Sci. USA* **2006**, *103*, 15729–15735.

[2] Liang, Y. Y.; Li, Y. G.; Wang, H. L.; Zhou, J. G.; Wang, J.; Regier, T.; Dai, H. J. Co_3O_4 nanocrystals on graphene as a synergistic catalyst for oxygen reduction reaction. *Nat. Mater.* **2011**, *10*, 780–786.

[3] Jung, N.; Chung, D. Y.; Ryu, J.; Yoo, S. J.; Sung, Y.-E. Pt-based nanoarchitecture and catalyst design for fuel cell applications. *Nano Today* **2014**, *9*, 433–456.

[4] Strmcnik, D.; Uchimura, M.; Wang, C.; Subbaraman, R.; Danilovic, N.; van der Vliet, D.; Paulikas, A. P.; Stamenkovic, V. R.; Markovic, N. M. Improving the hydrogen oxidation reaction rate by promotion of hydroxyl adsorption. *Nat. Chem.* **2013**, *5*, 300–306.

[5] Feng, J.; Gong, M.; Kenney, M. J.; Wu, J. Z.; Zhang, B.; Li, Y. G.; Dai, H. J. Nickel-coated silicon photocathode for water splitting in alkaline electrolytes. *Nano Res.* **2015**, *8*, 1577–1583.

[6] Wang, C.; Waje, M.; Wang, X.; Tang, J. M.; Haddon, R. C.; Yan, Y. S. Proton exchange membrane fuel cells with carbon nanotube based electrodes. *Nano Lett.* **2004**, *4*, 345–348.

[7] Bashyam, R.; Zelenay, P. A class of non-precious metal composite catalysts for fuel cells. *Nature* **2006**, *443*, 63–66.

[8] Chen, Z. W.; Higgins, D.; Yu, A. P.; Zhang, L.; Zhang, J. J. A review on non-precious metal electrocatalysts for PEM fuel cells. *Energ. Environ. Sci.* **2011**, *4*, 3167–3192.

[9] Wang, R. Y.; Liu, J. G.; Liu, P.; Bi, X. X.; Yan, X. L.; Wang, W. X.; Meng, Y. F.; Ge, X. B.; Chen, M. W.; Ding, Y. Ultra-thin layer structured anodes for highly durable low-Pt direct formic acid fuel cells. *Nano Res.* **2014**, *7*, 1569–1580.

[10] Gasteiger, H. A.; Markovic, N. M. Just a dream—or future reality? *Science* **2009**, *324*, 48–49.

[11] Zheng, F. L.; Wong, W. T.; Yung, K. F. Facile design of Au@Pt core–shell nanostructures: Formation of Pt submonolayers with tunable coverage and their applications in electrocatalysis. *Nano Res.* **2014**, *7*, 410–417.

[12] Wang, D. L.; Xin, H. L. L.; Hovden, R.; Wang, H. S.; Yu, Y. C.; Muller, D. A.; DiSalvo, F. J.; Abruña, H. D. Structurally ordered intermetallic platinum–cobalt core–shell nanoparticles with enhanced activity and stability as oxygen reduction electrocatalysts. *Nat. Mater.* **2013**, *12*, 81–87.

[13] Debe, M. K. Electrocatalyst approaches and challenges for automotive fuel cells. *Nature* **2012**, *486*, 43–51.

[14] Lim, B.; Jiang, M. J.; Camargo, P. H. C.; Cho, E. C.; Tao, J.; Lu, X. M.; Zhu, Y. M.; Xia, Y. N. Pd–Pt bimetallic nanodendrites with high activity for oxygen reduction. *Science* **2009**, *324*, 1302–1305.

[15] Bing, Y. H.; Liu, H. S.; Zhang, L.; Ghosh, D.; Zhang, J. J. Nanostructured Pt-alloy electrocatalysts for PEM fuel cell oxygen reduction reaction. *Chem. Soc. Rev.* **2010**, *39*, 2184–2202.

[16] Zhou, X.; Qiao, J.; Yang, L.; Zhang, J. A review of graphene-based nanostructural materials for both catalyst supports and metal-free catalysts in PEM fuel cell oxygen reduction reactions. *Adv. Energ. Mater.* **2014**, *4*, 1301523.

[17] Jia, F. L.; Zhao, J. H.; Yu, X. X. Nanoporous Cu film/Cu plate with superior catalytic performance toward electro-oxidation of hydrazine. *J. Power Sources* **2013**, *222*, 135–139.

[18] Karim-Nezhad, G.; Jafarloo, R.; Dorraji, P. S. Copper (hydr) oxide modified copper electrode for electrocatalytic oxidation of hydrazine in alkaline media. *Electrochim. Acta* **2009**, *54*, 5721–5726.

[19] Jeon, T.-Y.; Watanabe, M.; Miyatake, K. Carbon segregation-induced highly metallic Ni nanoparticles for electrocatalytic oxidation of hydrazine in alkaline media. *ACS Appl. Mater. Interfaces* **2014**, *6*, 18445–18449.

[20] Sanabria-Chinchilla, J.; Asazawa, K.; Sakamoto, T.; Yamada, K.; Tanaka, H.; Strasser, P. Noble metal-free hydrazine fuel cell catalysts: EPOC effect in competing chemical and electrochemical reaction pathways. *J. Am. Chem. Soc.* **2011**, *133*, 5425–5431.

[21] Sakamoto, T.; Asazawa, K.; Sanabria-Chinchilla, J.; Martinez, U.; Halevi, B.; Atanassov, P.; Strasser, P.; Tanaka, H. Combinatorial discovery of Ni-based binary and ternary catalysts for hydrazine electrooxidation for use in anion exchange membrane fuel cells. *J. Power Sources* **2014**, *247*, 605–611.

[22] Zhong, X.; Yang, H. D.; Guo, S. J.; Li, S. W.; Gou, G. L.; Niu, Z. Y.; Dong, Z. P.; Lei, Y. J.; Jin, J.; Li, R. *In situ* growth of Ni–Fe alloy on graphene-like MoS2 for catalysis of hydrazine oxidation. *J. Mater. Chem.* **2012**, *22*, 13925–13927.

[23] Burke, L.; O'Dwyer, K. Mediation of oxidation reactions at noble metal anodes by low levels of *in situ* generated hydroxy species. *Electrochim. Acta* **1989**, *34*, 1659–1664.

[24] Fukumoto, Y.; Matsunaga, T.; Hayashi, T. Electrocatalytic activities of metal electrodes in anodic oxidation of hydrazine in alkaline solution. *Electrochim. Acta* **1981**, *26*, 631–636.

[25] Ye, L. Q.; Li, Z. P.; Qin, H. Y.; Zhu, J. K.; Liu, B. H. Hydrazine electrooxidation on a composite catalyst consisting of nickel and palladium. *J. Power Sources* **2011**, *196*, 956–961.

[26] Lu, Z. Y.; Sun, M.; Xu, T. H.; Li, Y. J.; Xu, W. W; Chang, Z.; Ding, Y.; Sun, X. M.; Jiang, L. Superaerophobic electrodes for direct hydrazine fuel cells. *Adv. Mater.* **2015**, *27*, 2361–2366.

[27] Chen, C.; Kang, Y. J.; Huo, Z. Y.; Zhu, Z.; Huang, W. Y.; Xin, H. L. L.; Snyder, J. D.; Li, D. G.; Herron, J. A.; Mavrikakis, M. et al. Highly crystalline multimetallic nanoframes with three-dimensional electrocatalytic surfaces. *Science* **2014**, *343*, 1339–1343.

[28] Wang, Y.; Chen, Y. G.; Nan, C. Y.; Li, L. L.; Wang, D. S.; Peng, Q.; Li, Y. D. Phase-transfer interface promoted corrosion from $PtNi_{10}$ nanoctahedra to Pt_4Ni nanoframes. *Nano Res.* **2015**, 8, 140–155.

[29] Hu, C. G.; Cheng, H. H.; Zhao, Y.; Hu, Y.; Liu, Y.; Dai, L. M.; Qu, L. T. Newly-designed complex ternary Pt/PdCu nanoboxes anchored on three-dimensional graphene framework for highly efficient ethanol oxidation. *Adv. Mater.* **2012**, *24*, 5493–5498.

[30] Liu, H.-L.; Nosheen, F.; Wang. X. Noble metal alloy complex nanostructures: Controllable synthesis and their electrochemical property. *Chem. Soc. Rev.* **2015**, *44*, 3056–3078.

[31] Xiao, B.; Niu, Z. Q.; Wang, Y.-G.; Jia, W.; Shang, J.; Zhang, L.; Wang, D. S.; Fu, Y.; Zeng, J.; He, W. et al. Copper nanocrystal plane effect on stereoselectivity of catalytic deoxygenation of aromatic epoxides. *J. Am. Chem. Soc.* **2015**, *137*, 3791–3794.

[32] Lee, I.-S.; Kim, D.-H.; Kim, H.-E.; Jung, Y.-C.; Han, C.-H. Biological performance of calcium phosphate films formed on commercially pure Ti by electron-beam evaporation. *Biomaterials* **2002**, *23*, 609–615.

[33] Lu, Z. Y.; Chang, Z.; Zhu, W.; Sun, X. M. Beta-phased $Ni(OH)_2$ nanowall film with reversible capacitance higher than theoretical Faradic capacitance. *Chem. Commun.* **2011**, *47*, 9651–9653.

[34] Hou, J. X.; Kuang, Y.; Shen, H. Q.; Cao, H.; Luo, L.; Liu, J. F.; Wan, P. B.; Chen, B. Q.; Sun, X. M.; Tan, T. W. Solvothermal synthesis of FeCo nanoparticles for magneto-controllable biocatalysis. *RSC Adv.* **2014**, *4*, 11136–11141.

[35] Lu, Z.; Zhu, W.; Yu, X.; Zhang, H.; Li, Y.; Sun, X.; Wang, X.; Wang, H.; Wang, J.; Luo, J. Ultrahigh hydrogen evolution performance of under-water "superaerophobic" MoS_2 nanostructured electrodes. *Adv. Mater.* **2014**, *26*, 2683–2687.